Interactions of Intense Laser Radiation with Plasma [and Discussion]

M. H. Key and I. J. Spalding

Phil. Trans. R. Soc. Lond. A 1981 **300**, 599-612
doi: 10.1098/rsta.1981.0088

Phil. Trans. R. Soc. Lond. A **300**, 599–612 (1981) [599]
Printed in Great Britain

Interactions of intense laser radiation with plasma

By M. H. Key
S.R.C. Rutherford & Appleton Laboratories, Chilton, Didcot, Oxfordshire OX11 0QX, U.K.

The dominant physical processes involved in the interaction of intense laser radiation with plasma are discussed with emphasis on their dependence on the wavelength of the laser radiation. Hydrodynamic pressure resulting from these interactions, acceleration of spherical shell targets, and fluid instability associated with the acceleration are discussed with reference to compression of plasma in laser driven implosions. Experimental data are presented to illustrate the various phenomena.

1. Introduction

A major motivation in the study of the interaction of intense laser radiation with plasma arises from the possibility of compressing plasma to extreme density and pressure in spherically symmetric laser driven implosions. Recent work has shown that significant improvements in compression would result from irradiation with shorter laser-wavelength λ. This paper gives a brief summary of the arguments and the experimental evidence in favour of shorter wavelength.

2. Absorption

(*a*) *Collisional absorption*

Laser irradiation of a spherical target leads to the development of a steady-state radial flow of plasma with the characteristics shown schematically in figure 1 (Key 1980). The laser radiation penetrates the flow only to the point where the electron number density reaches the critical density n_c, where, for laser wavelength λ in micrometres,

$$n_c = 10^{21}\lambda^{-2}\ \text{electrons cm}^{-3}, \tag{1}$$

at which point reflexion occurs. The radial variation of density in the flow at sub-critical density where the flow velocity is approximately constant is of the form

$$n(r) = (r_c/r)^2 n_c, \tag{2}$$

where r_c is the radius at the critical density.

Absorption of the incoming laser radiation by electrons in binary collisions with ions (inverse bremsstrahlung) gives an absorption coefficient $K_{\text{i.b.}}$ which Hughes (1975) expresses as

$$K_{\text{i.b.}} = \frac{3\times10^5\,Z}{\lambda^2 T_e^{\frac{3}{2}}}\left(\frac{n_e}{n_c}\right)^2\left(1-\frac{n_e}{n_c}\right)^{-\frac{1}{2}}\text{cm}^{-1}, \tag{3}$$

for a plasma with ion charge Z, electron temperature T_e in electronvolts and laser wavelength λ in micrometres. The total absorption by inverse bremsstrahlung can be estimated by evaluating the opacity $\tau = 2\int_\infty^{r=r_c} K_{\text{i.b.}}\,\mathrm{d}r$ which from equations (2) and (3), together with equation (13) relating electron temperature to laser irradiance I, can be written as

$$\tau = 10^{-4}\frac{r_c}{\lambda^4}\frac{Z}{10^{-14}I}, \tag{4}$$

where r_c and λ are in micrometres and I is in watts per square centimetre. Equation (4) defines conditions in which collisional absorption dominates, i.e. $\tau \geqslant 1$. A typical set of parameters for which $\tau \geqslant 1$ is $Z \geqslant 30$, $r_c \geqslant 200\,\mu\text{m}$, $I \leqslant 10^{14}$, $\lambda \leqslant 1\,\mu\text{m}$. The importance of short laser-wavelength λ in obtaining efficient collisional absorption is seen in the λ^{-4} scaling of τ in equation (4). Conversely, collisional absorption becomes ineffective typically for $Z \leqslant 10$, $r \leqslant 100\,\mu\text{m}$, $I \geqslant 10^{14}\,\text{W cm}^{-2}$, and $\lambda \geqslant 1\,\mu\text{m}$. A significant fraction of the laser radiation then reaches the critical density, with two important consequences.

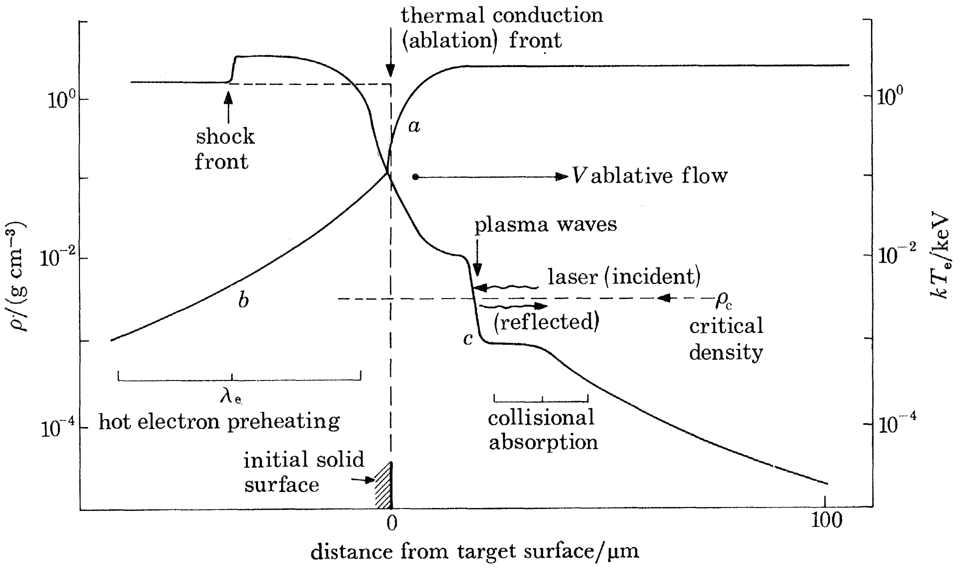

FIGURE 1. A schematic diagram showing features of a laser produced plasma. The magnitudes of the parameters are roughly appropriate to irradiation at $10^{15}\,\text{W cm}^{-2}$ with wavelength $\lambda = 1\,\mu\text{m}$. *a*, Ablation pressure; *b*, preheat pressure; *c*, light pressure. (After Key 1980.)

(*b*) *Density-profile steepening*

One effect of radiation reaching the critical density is a modification of the density profile of the flowing plasma due to the radiation pressure P_r as shown in figure 1.

R. E. Kidder (Proceedings, Japan–U.S. Seminar on Laser Interactions with Matter, unpublished (1972)) discussed this and showed that the plasma acceleration due to the radiation pressure is

$$\dot{u} = \tfrac{1}{2}\rho(n_e/n_c)\,\nabla(I/c), \tag{5}$$

for plasma of density ρ. This causes a jump in density at the critical density, where $\nabla(I/c)$ is large as the irradiance drops rapidly to zero. The jump $\Delta\rho$ is

$$\Delta\rho/\rho = (P_r/P_p)^{\frac{1}{2}}, \tag{6}$$

where P_p is the thermal pressure of the plasma. The ratio P_r/P_p is influenced by the 'swelling' of the radiation pressure P_r close to the critical density which arises as the group velocity of the wave tends to zero. The swelling factor $S = (1-n_e/n_c)^{-\frac{1}{2}}$ but has no singularity at $n_e \rightarrow n_c$ as shown by full solutions of the wave equation (see, for example, Mulser & Van Kessel 1977), being limited to an increase to several times the free space value of $P_r = I/c$. The plasma pressure at the critical density is $P_p = n_c kT_e$, and with equation (13) for T_e together with equations (6) and (1) it follows that

$$P_r/P_p = 3\times 10^{-2} S(10^{-16} I\lambda^2)^{\frac{1}{3}}, \tag{7}$$

where I is in watts per centimetre and λ in micrometres. The ratio of the radiation pressure to the thermal pressure thus depends on the parameter $I\lambda^2$ and becomes smaller for shorter wavelengths with the result that density profile steepening (equation (6)) is reduced.

The density jump occurs over a scale length that is typically sub-micrometre, and experimental measurement of this phenomenon has been achieved recently by short-pulse interferometric probing of laser produced plasmas. An example of this from experiments at the S.R.C. Central Laser Facility by Raven & Willi (1979) is shown in figure 2, and figure 3, from Willi *et al.* (1980), shows how their and other data give the dependence of $\Delta\rho/\rho$ on I.

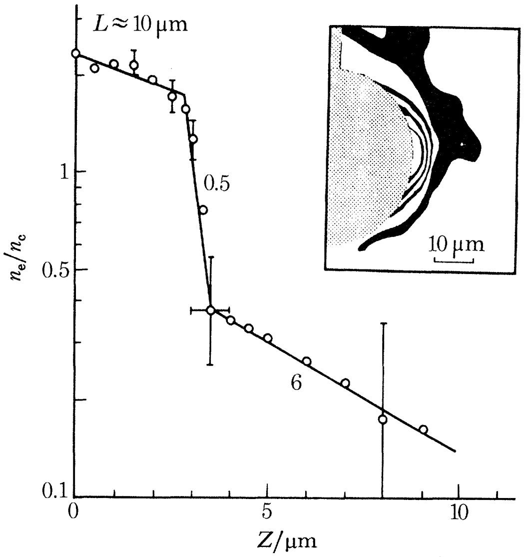

FIGURE 2. An experimental measurement of density profile steepening. The inset shows an interferogram of a spherical target being irradiated at 10^{16} W cm^{-2} by a 100 ps pulse of wavelength 1.06 µm. The graph shows the profile of electron number density along the direction of the laser beam. (After Raven & Willi 1979.)

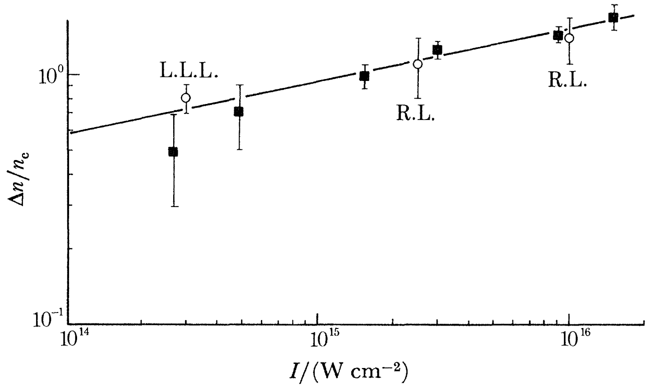

FIGURE 3. The magnitude of the light pressure induced electron density step for $\lambda = 1$ µm. ○, Measurements from interferometry. ■, Computer calculations. R.L., Rutherford Laboratory; L.L.L., Lawrence Livermore Laboratory. (After Willi *et al.* 1980.)

(*c*) *Brillouin scattering*

Density profile steepening is a non-resonant hydrodynamic effect. Radiation pressure can also drive natural hydrodynamic resonances in the plasma, as when it couples with accoustic waves in stimulated Brillouin scattering. Figure 4 shows schematically how this occurs. The plasma in the sub-critical density flow has an approximately constant temperature (Key 1980) and therefore a constant sound velocity V_a. A sound wave travelling at V_a, which modulates the plasma density at a wavelength satisfying the requirement for Bragg reflexion of the laser light at ω_0, gives a Döppler shifted back-scattered wave at $\omega_0 - \omega_a$ where ω_0 is the laser frequency and ω_a is the sound-wave frequency. The interaction of the back-scattered and incident waves creates a 'standing' wave pattern which moves at the sound velocity V_a. The radiation forces on the plasma (see equation (5)) drive the plasma away from the antinodes of the standing wave, resonantly increasing the amplitude of the sound wave and, therefore, its reflectivity for the laser radiation.

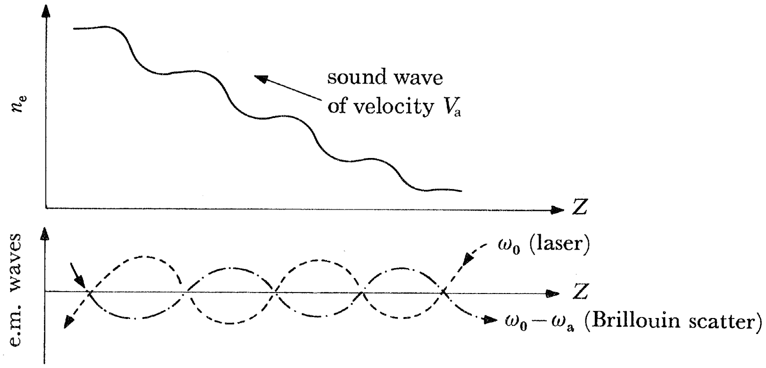

FIGURE 4. Schematic diagram of physical processes in stimulated Brillouin back-scattering. Laser radiation is incident from the right at frequency ω_0 in a plasma where the sound wave velocity is V_a. A sound wave of frequency ω_a modulates the electron number density profile with a periodicity such that Bragg reflexion causes Doppler shifted back-scattering at frequency ω_0–ω_a.

This resonant positive feedback drives the wave amplitude to a saturated level giving stimulated Brillouin scattering. This may reflect a large fraction of the incident laser radiation since it occurs at sub-critical density while most absorption occurs very close to critical density (equation (2)). The threshold for the process in a plasma where density decreases from n_e with a scale length L has been computed by Rosenbluth (1972) and can be written as

$$I > 10^{13} T_e L^{-1} \lambda^{-1} (n_e/n_c)^{-1}\,\mathrm{W\,cm^{-2}}, \tag{8}$$

where T_e is in electronvolts and L and λ are in micrometres. Reducing the laser wavelength λ is thus seen to increase the threshold for stimulated Brillouin scattering. Even where the irradiance threshold is exceeded the scattering may not develop if absorption by inverse bremsstrahlung attenuates the radiation before n_e/n_c is large enough for Brillouin scattering. This can occur in high-Z plasmas and particularly with short laser-wavelength since from equations (8), (2) and (3), and from Evans (1980), quenching of stimulated Brillouin scattering by inverse bremsstrahlung absorption will occur if

$$I < 2 \times 10^{14} Z \lambda^{-3} T_e^{-\frac{1}{2}}\,\mathrm{W\,cm^{-2}} \tag{9}$$

for λ in micrometres and T_e in electronvolt. Here again reducing λ suppresses Brillouin scattering. There is some experimental evidence supporting the foregoing scaling arguments. Brillouin scattering is typically identified as a red-shifted reflexion from laser produced plasmas as illustrated in figure 5 which shows a time resolved spectrum of back-scattered radiation when a plane target is irradiated by 0.53 μm light at *ca.* $4 \times 10^{15}\,\mathrm{W\,cm^{-3}}$ (Cole *et al.* 1980). Back-scattering is only 3 % in the above experiment compared to *ca.* 20 % in similar observations with $\lambda = 1.05$ μm. Other work by, for example, Phillion *et al.* (1977) and Ripin & McClean (1978) has shown up to 40 % back-scatter for 1.06 μm irradiation. There remains uncertainty whether Brillouin scattering can be adequately suppressed when larger targets with larger plasma scale-lengths are irradiated in laser fusion experiments (Estabrook, K. & Harte, J. 1979, Lawrence Livermore Laboratory Preprint UCRL 82620, Rev. 2, unpublished).

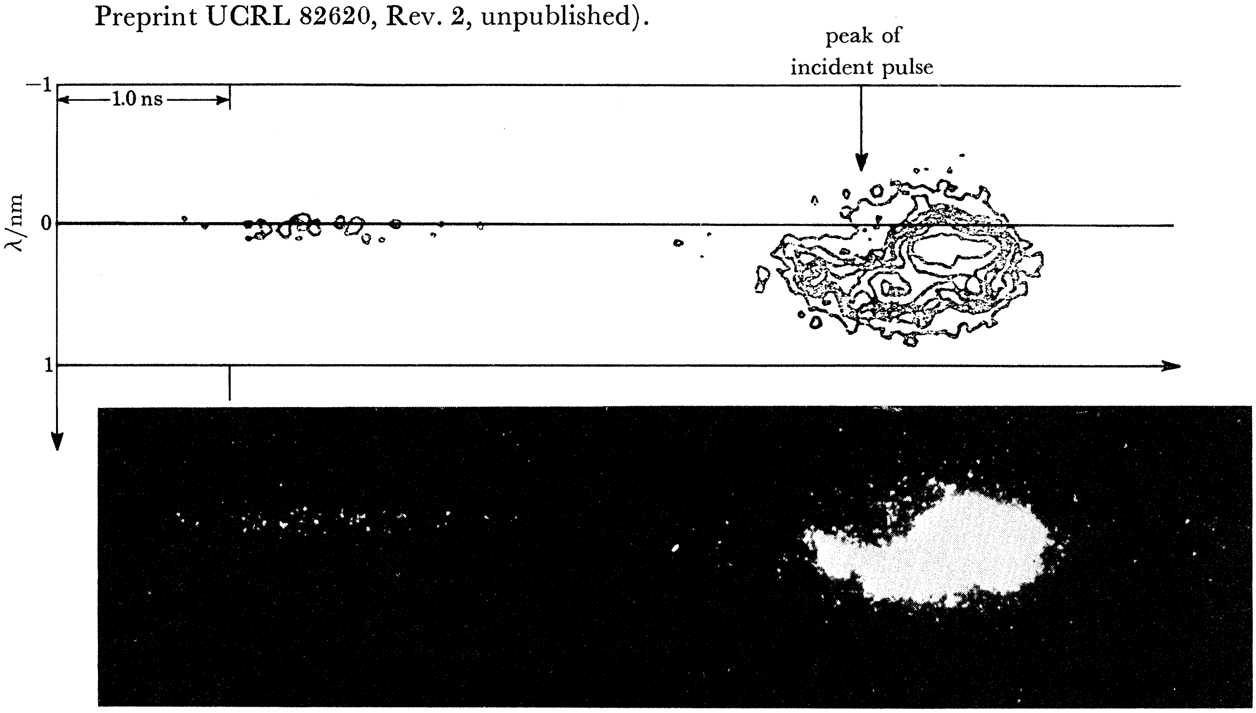

FIGURE 5. A streak time resolved spectrum of back-scattered laser radiation from a tungsten target at 45° irradiated at 4×10^{15} W cm^{-2} at 1 ns pulse duration with $\lambda = 0.53$ μm. The figure shows the streak picture (below) and a contour densitometer tracing of it (above). A fraction of the incident beam is recorded by the streak camera before the back-scattered radiation and has a narrow spectral bandwidth centred at ω_0. The back-scattered radiation is seen to be red-shifted by approximately 0.3 nm and broadened in frequency. The red shift is the Brillouin Doppler shift. (After Cole *et al.* 1980.)

(*d*) *Resonance absorption*

An important corollary of the formation of a density step at the critical density for high values of $I\lambda^2$ is the process of resonance absorption (Freidberg *et al.* 1972) which leads to up to 33 % absorption independent of collisions and, therefore, of the plasma temperature and laser irradiance. The mechanism is illustrated schematically in figure 6. P-polarized radiation incident obliquely (at angle θ) on a plasma with a steep density gradient is refracted, and at its turning point it has an axially directed $\boldsymbol{E}$-vector. The electric field can tunnel from the turning point at $n_e = n_c \cos^2\theta$ to the critical density, where there is a singularity in its magnitude in the solution of the wave equation. The electric-field drives resonant plasma oscillations, and Landau damping or wave breaking limits the wave amplitude. The damping gives energy only to the high energy tail of the electron energy distribution function, individual electrons moving with the wave acquiring energy ϵ of the order eEL, where E is the axial field and L the scale length of the density gradient.

Maximum resonance absorption occurs when the angle of incidence is given by

$$\sin^2\theta_0 = 0.6(2\pi L/\lambda)^{-\frac{2}{3}}. \tag{10}$$

This is a compromise between oblique incidence giving a greater axial $\boldsymbol{E}$-vector and perpendicular incidence taking the turning point closer to the critical density. Since focused laser beams have a typical angle range of ± 25° the process is effective when $\theta_0 \nless 25°$, requiring $L \ngtr \lambda$. Since profile steepening gives $L \sim \lambda$ it follows that the heated electron energy should scale as $(I\lambda^2)^{\frac{1}{2}}$. It has been found experimentally that for values of $I\lambda^2$ exceeding about $10^{14}\,\mathrm{W\,cm^{-2}\,\mu m^2}$ the plasma has a small percentage of hot electrons with a temperature T_h several times greater than the bulk temperature. Their temperature can be deduced from the slope of the X-ray bremsstrahlung spectrum radiated by them, and it originates in the damping of plasma waves as discussed above. Figure 7 from Amiranov *et al.* (1979) shows that this hot electron temperature scales with

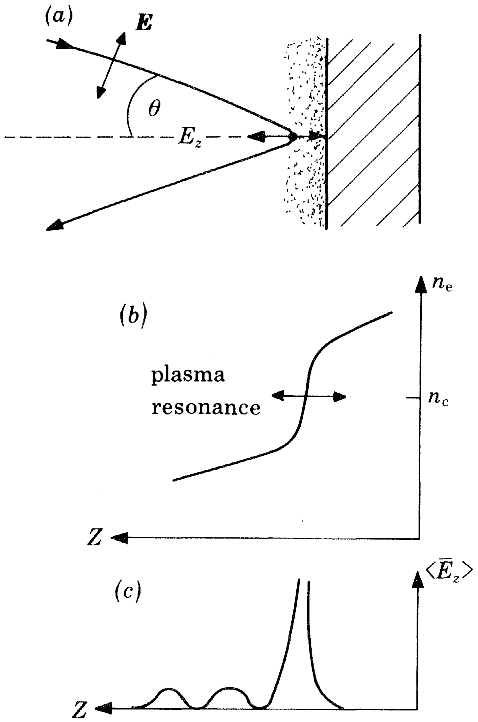

FIGURE 6. A schematic diagram of physical processes in resonance absorption. (*a*) P-polarized laser radiation incident at angle θ on a plane target giving an axial electric field E_z at the turning point. The magnitude of E_z, shown in (*c*), has a resonance at the point where the electron number density, shown in (*b*), is equal to the critical density. Resonantly driven plasma oscillations occur at this point.

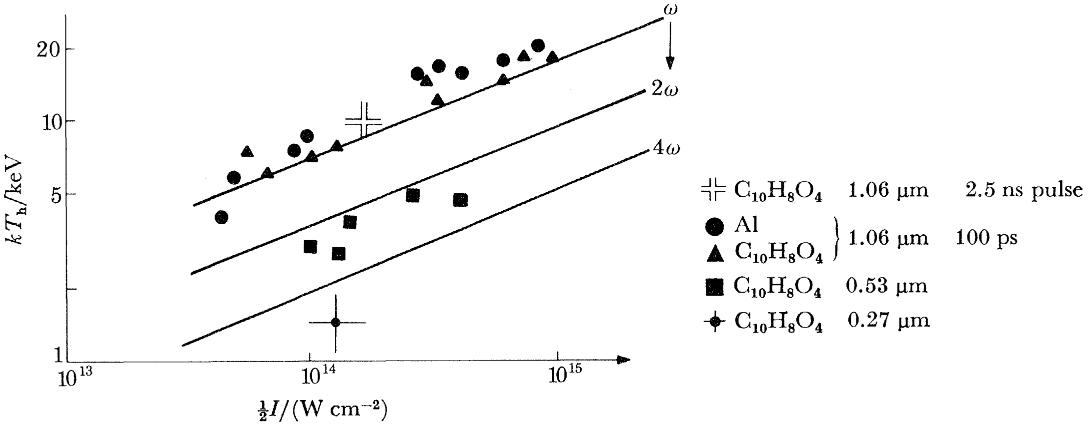

FIGURE 7. Hot electron temperature as a function of irradiance and wavelength. Data are shown for laser radiation at ω (λ = 1.06 μm), 2ω and 4ω. The top solid line shows the average experimental scaling at ω, and the lower solid lines for 2ω and 4ω are shifted by assuming that kT_h is a function of $I\lambda^2$. (After Amiranov *et al.* 1979.)

irradiance and wavelength approximately as $(I\lambda^2)^{\frac{1}{3}}$. The hot electron temperature is thus reduced by reducing λ. The significance of this wavelength scaling is considered further below.

(*e*) *Summary of absorption processes*

There has been considerable effort devoted to measurement of the net absorption by all processes as a function of parameters such as irradiance, wavelength and pulse length. Figure 8, from the recent work of Amiranov *et al.* (1979), shows, for example, how absorption is generally greater for shorter wavelengths and falls with reduction of pulse length except in the limit of high irradiance where the longer pulses generate greater plasma scale-length and more Brillouin scattering.

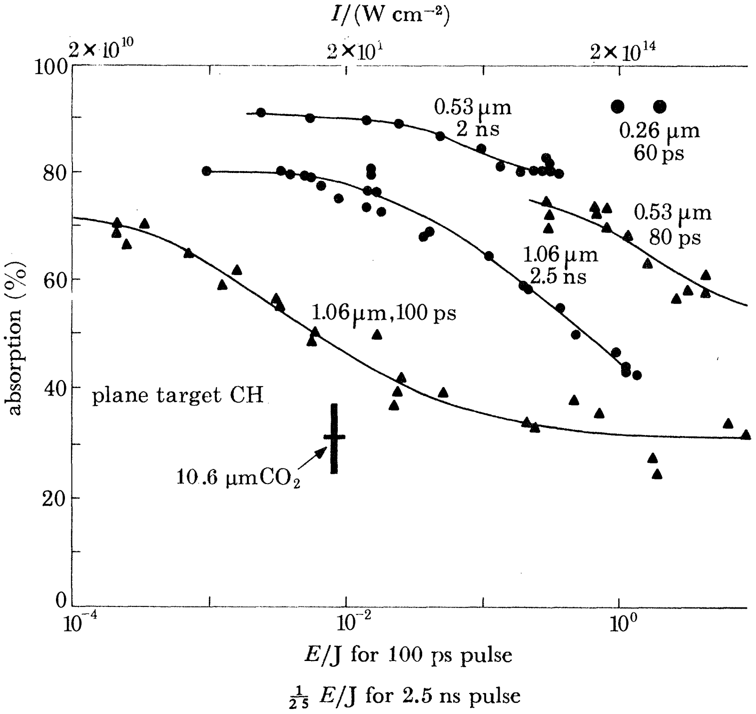

FIGURE 8. Measurements of the absorption as a function of irradiance for λ = 0.26, 0.53, 1.06 and 10.6 μm, (the latter labelled CO_2). Data are for different pulse durations as indicated. (After Amiranov *et al.* 1979.)

3. PREHEATING BY HOT ELECTRONS, AND ITS EFFECT ON COMPRESSION

(*a*) *Range of hot-electron preheating*

The hot electrons whose temperature T_h was considered in §2(*d*) may carry a significant fraction of the absorbed laser energy. Their range is typically large compared with the scale of the high temperature plasma (see figure 1) so that they deposit energy in the cold solid-density material ahead of the thermal conduction front formed by most of the plasma electrons. Most energy flow in a Maxwellian distribution is due to particles with $\epsilon \approx 3\,kT$ so that inspection of figure 7 shows that hot electrons with energies of the order of 30 keV dominate the hot electron transport when $I\lambda^2 \approx 3 \times 10^{14}\,W\,cm^{-2}\,\mu m^2$. A 30 keV electron has a range λ_e in matter of density of the order of $2 \times 10^{-3}\,g\,cm^{-2}$. Since the range scales roughly quadratically with energy it follows that $\lambda_e \approx T_h^2$ and, from figure 7, that

$$\lambda_e \approx 10^{-3} \times 10^{-14} I\lambda^2\,g\,cm^{-2}, \tag{11}$$

where λ is in micrometres and I is in watts per square centimetre. The range λ_e is a measure of how far preheating by hot electrons extends into a target. If the target is a spherical shell with a wall of thickness $\rho\Delta r$ g cm^{-2} then unless $\rho\Delta r > \lambda_e$ there will be significant preheating of the contents of the spherical shell before any compression induced by implosion of the shell.

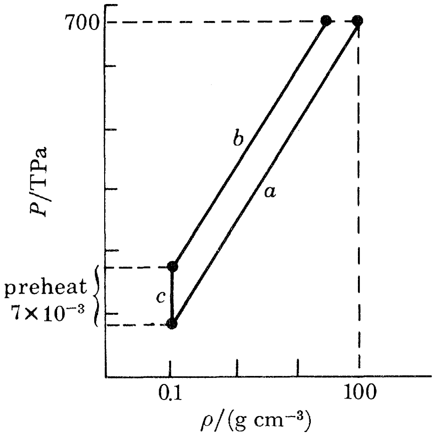

FIGURE 9. An illustration of the effect of preheating on compression: line *a*, for a Fermi degenerate electron gas compressed from 0.1 to 100 g cm^{-3}; line *b* for a compression to the same final pressure but with preheating (line *c*) equivalent to 3 % of compressive work.

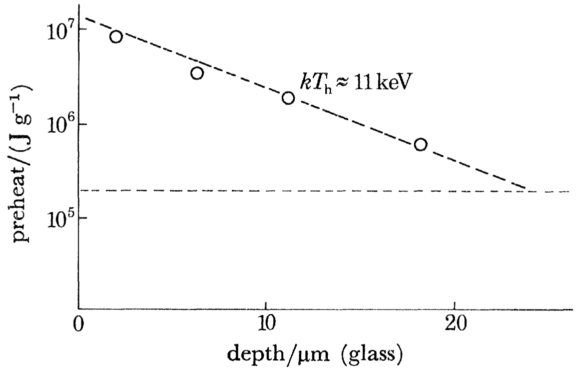

FIGURE 10. Preheating by hot electrons as a function of depth in a solid target. Data points are from Hares *et al.* (1979) for 2×10^{15} W cm^{-2} irradiation at $\lambda = 1.06$ µm, giving $kT_h = 11$ keV. Horizontal line is preheat level assumed in figure 9, giving a two-fold reduction of compressed density.

Compression to high density in implosions may be seriously impaired by preheating. The maximum density for a given pressure can be estimated from the Fermi degenerate pressure of electrons by assuming a fully ionized plasma with a mass content of 2 u per electron ($\mathrm{u} \approx 1.661\times10^{-27}$ kg) and is

$$\rho \leqslant 0.5(10^{-12}P)^{\frac{3}{5}}\ \mathrm{g\ cm^{-3}} \tag{12}$$

from pressure P in dyn cm^{-2}. This is applicable for low-Z plasmas at pressures above several megabars. (Mbar $= 10^{12}$ dyn cm^{-2} $= 10^{-1}$ TPa) figure 9 shows how this simple model indicates that a pressure of 700 TPa is required to reach a Fermi degenerate density of 100 g cm^{-3}. It also shows how, if the compression were ideally adiabatic from 0.1 g cm^{-3}, an initial preheating equivalent to only 3 % of the work done in compression degrades the final density at 700 TPa from 100 to 50 g cm^{-3}. This corresponds to preheating of 2×10^5 J g^{-1} at 0.1 g cm^{-3}.

It is clear from equation (11) that reducing the laser wavelength will reduce the range of preheating but it is important also to measure its magnitude and range. Hares *et al.* (1979) showed how hot electron preheating could be measured from the total K_α fluorescence from various elements in layered targets. The experiment involved 100 ps pulse irradiation at $I\lambda^2 \approx 2 \times 10^{15}$ W cm^{-2} μm^2, and the hot electron energies greatly exceeded the ionization threshold of K electrons in Ca and K which were used as K_α fluors. Figure 10 shows the measured preheating in joules per gram as a function of depth (expressed in units of micrometres of glass). Also shown is the pre-heating level of 2×10^5 J g^{-1} which would lead to a twofold loss of compression in 700 TPa compression from 0.1 g cm^{-3} as discussed above. Clearly the target shell would need to be about 25 μm thick if $I\lambda^2 \approx 2 \times 10^{15}$ W cm^{-2} μm^2; for thinner shells $I\lambda^2$ would have to be reduced proportionately. The shell thickness is an important parameter in the hydrodynamics of spherical implosions for reasons other than preheating, and the fact that preheating puts a further constraint on it is discussed in § 5.

4. Ablation

Since absorption of laser radiation occurs primarily close to the critical density the first-order effect of irradiation is to create hot plasma with an initial density of the order of the critical density. The high pressure of the plasma causes expansion into vacuum at a velocity of the order of the ion thermal velocity. This process has been termed ablation and there is a high pressure exerted on the target by the combined effect of thermal pressure and momentum transfer due to the reaction to the flow. The pressure is the ablation pressure P_a and, for sonic flow at the critical density, simple energy and momentum conservation equations show (see, for example, Key 1979) that the temperature T_a and pressure P_a are given by

$$kT_a = 3.3\lambda^{\frac{4}{3}}(10^{-14}I)^{\frac{2}{3}}\,\text{keV}, \tag{13}$$

$$P_a \approx 1.4(10^{-14}I)^{\frac{2}{3}}\,\lambda^{-\frac{2}{3}}\,\text{TPa}, \tag{14}$$

for I in watts per square centimetre and λ in micrometres. It also follows from equation (14) that if $I\lambda^2$ is constrained to a fixed value by the preheating considerations discussed above then the maximum useful ablation pressure $P_{\text{a.m.}}$ is of the order

$$P_{\text{a.m.}} = 1.4\lambda^{-2}\,\text{TPa}, \tag{15}$$

where λ is in micrometres and it has been assumed that $I\lambda^2 = 10^{14}$ W cm^{-2} μm^2. The very strong scaling of maximum pressure with laser wavelength in equation (15) suggests a major advantage for short wavelength lasers in ablative compression. The model presented above is simple rather than exact: in particular because it ignores thermal conduction which carries the heat front to densities higher than the critical density as shown schematically in figure 1. The final conclusion on the ablation pressure is best drawn from experiments, and recent work at the S.R.C. Central Laser Facility (Key *et al.* 1980) has given the first direct comparison of ablation pressure for 1.05 μm and 0.53 μm irradiation. The experiments involved a new method of pressure determination based on the momentum conservation relation

$$P_a = \dot{m}V_i, \tag{16}$$

where $\dot{m}$ is the mass ablation rate and V_i the limiting velocity of the ablated ions at a large distance from the target. The mass ablation rate $\dot{m}$ was deduced from the time taken for the high temperature thermal front to penetrate a known thickness of Al on an SiO_2 target. The time was measured by streak time-resolved X-ray spectroscopy showing the delay between emission from Al(XII) and Si(XIII) ions in high temperature plasma. V_i was obtained simply from the flight time of ions reaching a Faraday cup collector 50 cm from the target. The results shown in figure 11 demonstrate an ablation pressure three to four times greater at the same irradiance for 0.53 μm relative to 1.05 μm irradiation with up to 5 TPa pressure recorded at $I = 6 \times 10^{14}$ W cm^{-2}, confirming the advantage of short wavelength irradiation.

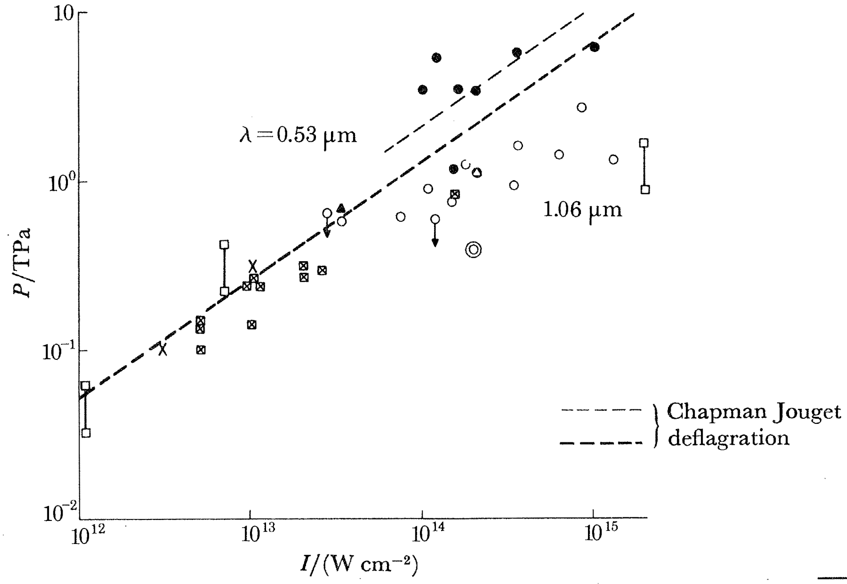

FIGURE 11. Ablation pressure as a function of irradiance for $\lambda = 1.06$ μm (open symbols) and 0.53 μm (filled symbols ●). Data from several sources are shown together with the analytic model prediction (– – –) of equation (14). ⊠, From Streak time resolved X-ray shadowgraphy; ● and ○, from time resolved mass ablation rates. (After Key *et al.* 1980.)

5. ABLATIVE IMPLOSIONS

(a) *Scaling analysis*

The above ablation pressure is used as the driving force in experiments where spherical shell targets with $\Delta r > \lambda_e$ are imploded to produce highly compressed plasma. This 'ablative compression' process makes it possible to study laboratory plasmas at hitherto inaccessible high densities and pressures, and is vital in laser fusion research. Maximizing the plasma density obtained in ablative compression requires low preheating and maximum pressure in the implosion core. If a spherical shell target is imploded to a maximum velocity V_m with a density ρ close to its initial solid density, and if the implosion stagnates at the centre of the sphere converting kinetic energy to pressure, the final pressure P_f is given approximately by

$$P_f = \rho V_m^2. \qquad (17)$$

By assuming constant acceleration over a distance of the order of the radius r for a shell of thickness Δr it follows that

$$P_f = 2(r/\Delta r)\, P_a, \qquad (18)$$

in the limit where only a small fraction $\Delta M/M$ of the shell mass is lost by ablation. Large aspect ratio $r/\Delta r$ is thus seen to cause a large pressure multiplication ratio P_f/P_a and is obviously desirable. The efficiency ϵ_h of converting absorbed energy to kinetic energy in the implosion in this simple rocket-like ablation process is readily shown (see, for example, Key 1979) to be

$$\epsilon_h \sim \Delta M/M. \qquad (19)$$

The ultimate limiting factor on shell aspect ratio would be complete burn-through of the shell ($\Delta M \rightarrow M$) in the case of very thin shells, but unstable break-up of the shell by the Rayleigh–Taylor acceleration instability will intervene sooner in most cases. The classical process is the growth of interface perturbations when a light fluid accelerates a dense fluid. The low density ablation plasma and the dense shell are thus classically unstable at their interface. It has been calculated (see, for example, Bodner *et al.* 1978) that the most rapid growth is for perturbations of wavelength $l \sim \Delta r$, with the result that for a growth rate $\gamma = 2\pi\ddot{r}/l$ the total growth exponent for the perturbations in acceleration of the shell through distance r reaches

$$\int \gamma \, \mathrm{d}t = (4\pi r/\Delta r)^{\frac{1}{2}}. \tag{20}$$

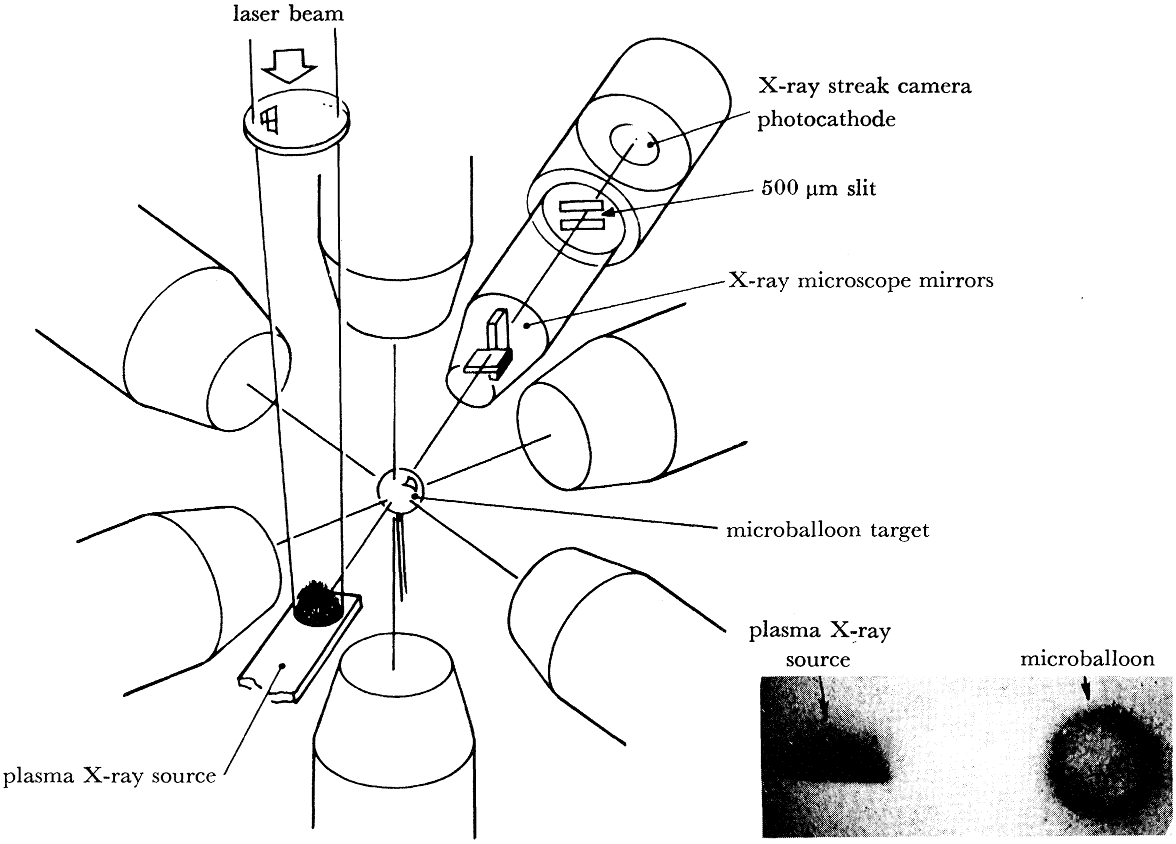

FIGURE 12. Schematic diagram of the apparatus used for six-beam ablative implosion studies with streak time resolved X-ray shadowgraphy diagnostics. The inset pinhole-camera picture shows the relative size and position of the plasma X-ray source and microballoon target.

The desirability of low $r/\Delta r$ for stability and high $r/\Delta r$ for pressure multiplication is apparent from equations (18) and (20). Here again experimental evidence is needed to determine the optimum value of $r/\Delta r$ since theoretical analysis of the problem in full detail is highly intractable. Short laser wavelengths are advantageous in ablative compression. If the shell thickness Δr is specified and thus $I\lambda^2$ determined from the condition $\lambda_e < \Delta r$ required for an ablative implosion, then it follows from the foregoing models of the ablation and implosion process that constant final pressure P_f and hydrodynamic efficiency ϵ_h are obtainable only if $r/\Delta r$ scales as λ^2. This means that greater problems with stability are incurred in achieving a given final pressure by using longer laser wavelength. Alternatively if the further constraint $r/\Delta r$ = const. is assumed as a stability requirement then $P_\mathrm{f} \sim \lambda^{-2}$ and $\epsilon_\mathrm{h} \sim \lambda^{-2}$, which suggests a rapid increase in attainable pressure by reducing the laser wavelength.

(*b*) *Experimental observation*

Experimental study of ablative implosions is more difficult than that of 'exploding pusher' targets (Attwood 1979). The latter are strong sources of X-ray line radiation and thermonuclear fusion particles which provide copious information about the plasma, but the higher density but lower temperature plasmas produced by ablative compression do not have these emission features.

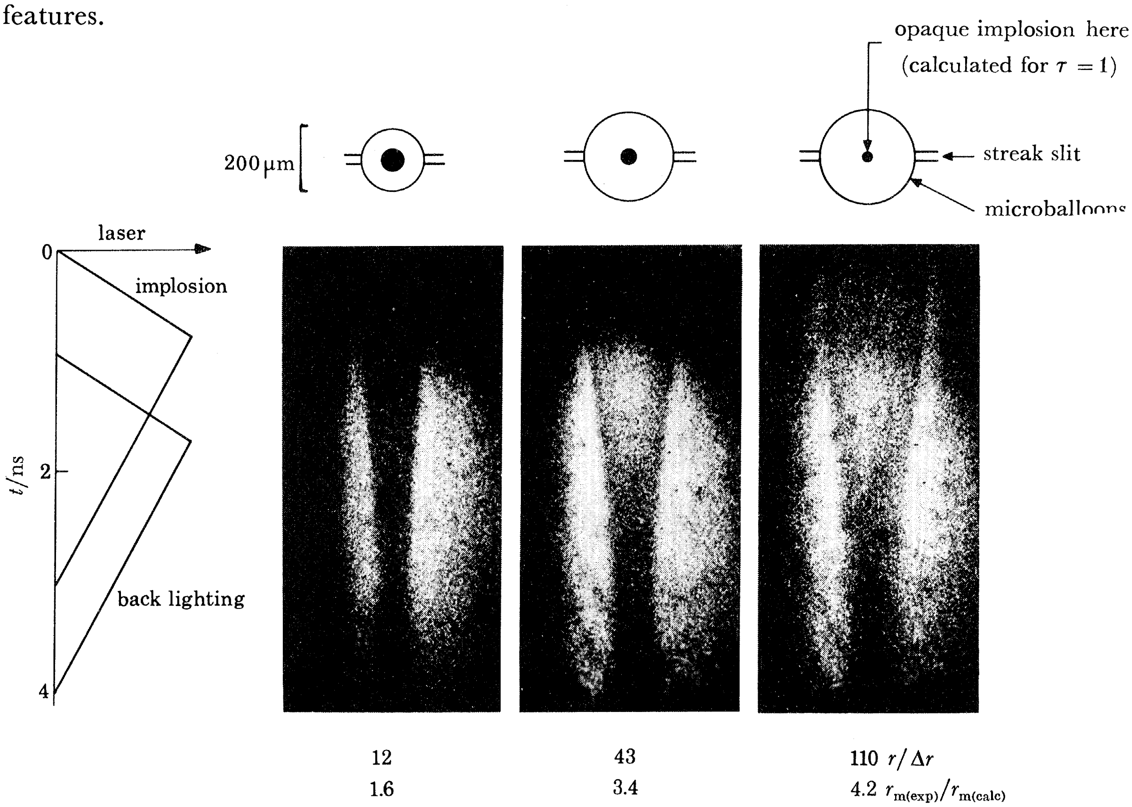

FIGURE 13. Three examples of ablative implosions diagnosed by streak time resolved X-ray shadowgraphy. The sketches above are scale drawings of the initial microballoon diameter, the streak slit and the computed size of the opaque compression core. The graph at the left side shows the relative timing of the irradiation of the microballoon and the back-lighting target. The streak pictures show the implosion trajectory and minimum size of the opaque core for shells of aspect ratio $r/\Delta r$ = 12, 43 and 110. The ratio $r_{\mathrm{m\ (exp)}}/r_{\mathrm{m\ (calc)}}$ is that of observed to computed minimum opaque core size. (After Key *et al.* 1980.)

Recent work in which the ablative implosion has been observed against an intense background source of soft X-rays from a second laser-produced plasma has given much improved diagnostic possibilities. There are several ways in which such X-ray backlighting experiments can diagnose ablative implosions. Two-dimensional images of the absorbing region in imploding shells are obtained if the X-ray pulse duration is short relative to the implosion time (Key *et al.* 1979). One-dimensional recording of the implosion trajectory is obtained by X-ray streak photography as in figure 12, from Key *et al.* (1980). The imploding target is imaged by an X-ray microscope onto the slit of an X-ray streak camera. Six laser beams irradiate the microballoon target and a seventh is focused onto a plane solid target to produce a plasma whose X-ray emission is much brighter than that of the microballoon. The trajectory of the absorption region in the microballoon target is seen in the streak records in figure 13 for targets with a range of aspect ratio between 12 and 110. Analysis of such data can give values for density in the implosion core, acceleration and therefore ablation pressure at the shell surface and evidence of unstable break-up of the shell. Ablation pressure results obtained in this way are shown in figure 11. Evidence of unstable behaviour is shown in figure 14 where the ratio of the observed to computer simulated volume of the implosion core is plotted as a function of $r/\Delta r$. The ratio increases rapidly with $r/\Delta r$ suggesting increasing degradation of the implosion due to unstable break up of the shell (which is not included in the one dimensional computer model).

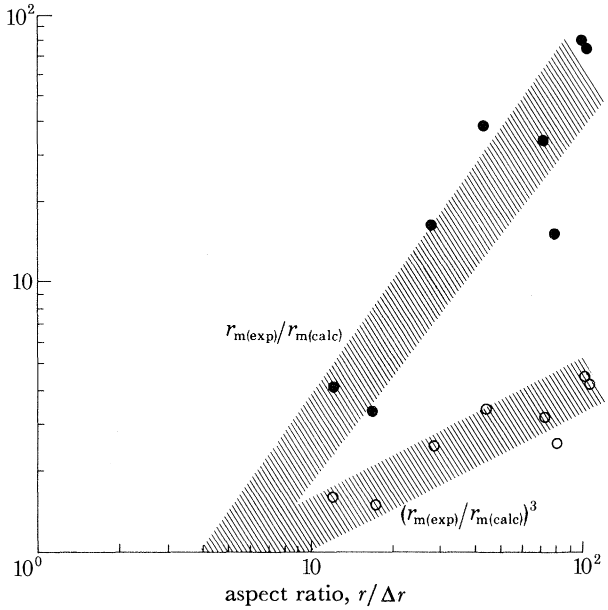

FIGURE 14. Ratio of observed to computed sizes of the opaque core for ablative implosions as a function of aspect ratio $r/\Delta r$. (After Key *et al.* 1980.)

The future prospects in this field are for much increased emphasis in research on the ablative mode of implosion. Plasma density of 40 g cm^{-3} and pressure of 2×10^{10} atmospheres (*ca.* 2×10^3 TPa) was achieved in February 1980 in the U.S.A. Shorter wavelength lasers of greater power will soon lead to improved compression, and much interest attaches to the implications for fusion power, as well as for fundamental physics.

REFERENCES (Key)

Amiranov, F. *et al.* 1979 21st Annual Meeting of Division of Plasma Physics, American Physical Society, Boston, U.S.A.

Bodner, S. E. *et al.* 1978 *Proceedings of the IAEA Conference on Plasma Physics and CTR Research.* Innsbruck, Austria, paper IAEA CM 37-B-3.

Cole, A., Murdoch, J., Sim, S. L. M. & Evans, R. G. 1980 *S.R.C. Rutherford Lab. Rep.* RL 80 026 and *Optics Commun.* (In the press.)

Evans, R. E. 1980 *S.R.C. Rutherford Lab. Rep.* RL 80 026 and *Plasma. Phys.* (In the press.)

Freidberg, J. P., Mitchell, R. W., Morse, R. L. & Rudinski, L. I. 1972 *Phys. Rev. Lett.* **28**, 795.

Hares, J. D., Kilkenny, J. D., Key, M. H. & Lunney, J. G. 1979 *Phys. Rev. Lett.* **42**, 1216.

Hughes, T. P. 1975 *Plasmas and laser light*, p. 45. Bristol: A. Hilger.

Key, M. H. 1979 *Proceedings of the 20th Scottish Universities Summer School in Physics, St Andrews.* S.U.S.S.P. Publications.

Key, M. H. 1980 *Phil. Trans. R. Soc. Lond.* A **298**, 351–364.
Key, M. H. *et al.* 1980 *S.R.C. Rutherford Lab. Rep.* RL 80 023 and *Phys. Rev. Lett.* **45**, 1801.
Key, M. H., Lewis, C. L. S., Lunney, J. G., Moore, A., Hall, T. A. & Evans, R. G. 1978 *Phys. Rev. Lett.* **41**, 1467.
Mulser, P. & Van Kessel, C. 1977 *Phys. Rev. Lett.* **38**, 902.
Phillion, D. W., Kruer, W. C. & Rupert, V. C. 1977 *Phys. Rev. Lett.* **39**, 1529.
Raven, A. & Willi, O. 1979 *Phys. Rev. Lett.* **43**, 278.
Ripin, B. H. & McLean, E. A. 1979 *Appl. Phys. Lett.* **34**, 809.
Rosenbluth, M. N. 1972 *Phys. Rev. Lett.* **29**, 565.
Willi, O., Evans, R. E. & Raven, A. 1980 *Physics Fluids.* **23**, 2061.

Discussion

I. J. Spalding (*U.K.A.E.A., Culham Laboratory, Abingdon, Oxfordshire OX*11 3*DB, U.K.*). Is the ablation pressure measured at a spherical target significantly different from that of a plane target, at the same incident irradiance and wavelength?

M. H. Key. Both types of geometry were used to obtain the data illustrated in the talk. The experimental results are broadly similar.

I. J. Spalding. The simple λ^2-scaling emphasized by Dr Key is a feature of analytic theories published in the period 1970–73; these tended to neglect the effects of ponderomotive forces (which are certainly important at $\lambda = 10\,\mu\text{m}$).

M. H. Key. What I have done is to compile some of the early analytic ideas together with recent experimental data. The latter define the ranges of usefulness of the analytic models. Furthermore, I have carried through the arguments to examine their impact on implosions. I think that the role of the ponderomotive force is considered in this discussion, where I have considered density profile steepening, resonance absorption and Brillouin scattering, and ephasized the basic $(I\lambda^2)^x$-scaling associated with these processes. In discussing ablation pressure the departure from the simple analytic model above an $I\lambda^2$-limit is also discussed and can be associated with the above $I\lambda^2$-dependent processes.

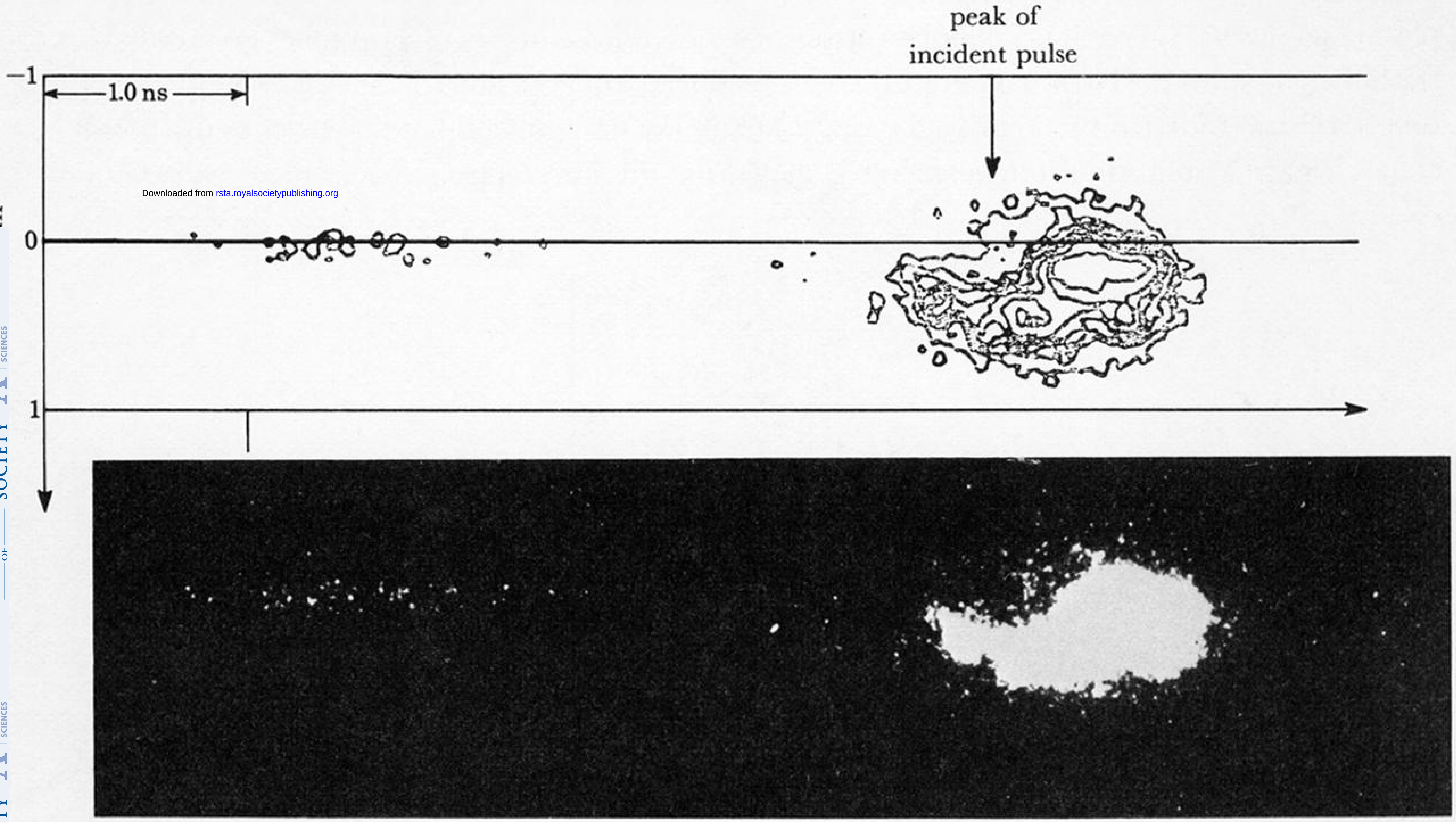

Figure 5. A streak time resolved spectrum of back-scattered laser radiation from a tungsten target at 45° irradiated at 4×10^{15} W cm^{-2} at 1 ns pulse duration with $\lambda = 0.53$ μm. The figure shows the streak picture (below) and a contour densitometer tracing of it (above). A fraction of the incident beam is recorded by the streak camera before the back-scattered radiation and has a narrow spectral bandwidth centred at ω_0. The back-scattered radiation is seen to be red-shifted by approximately 0.3 nm and broadened in frequency. The red shift is the Brillouin Doppler shift. (After Cole *et al.* 1980.)

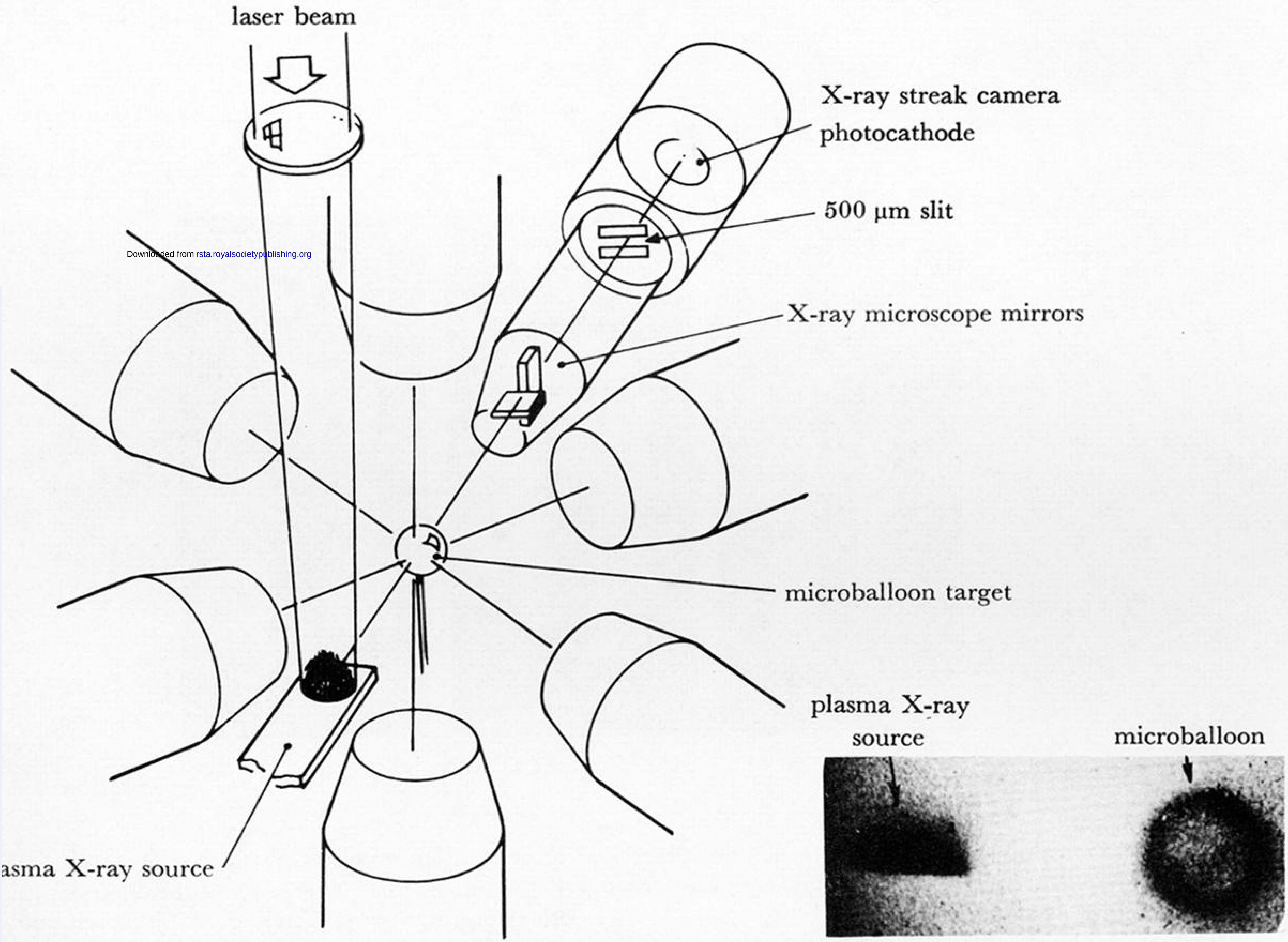

IGURE 12. Schematic diagram of the apparatus used for six-beam ablative implosion studies with streak time resolved X-ray shadowgraphy diagnostics. The inset pinhole-camera picture shows the relative size and position of the plasma X-ray source and microballoon target.

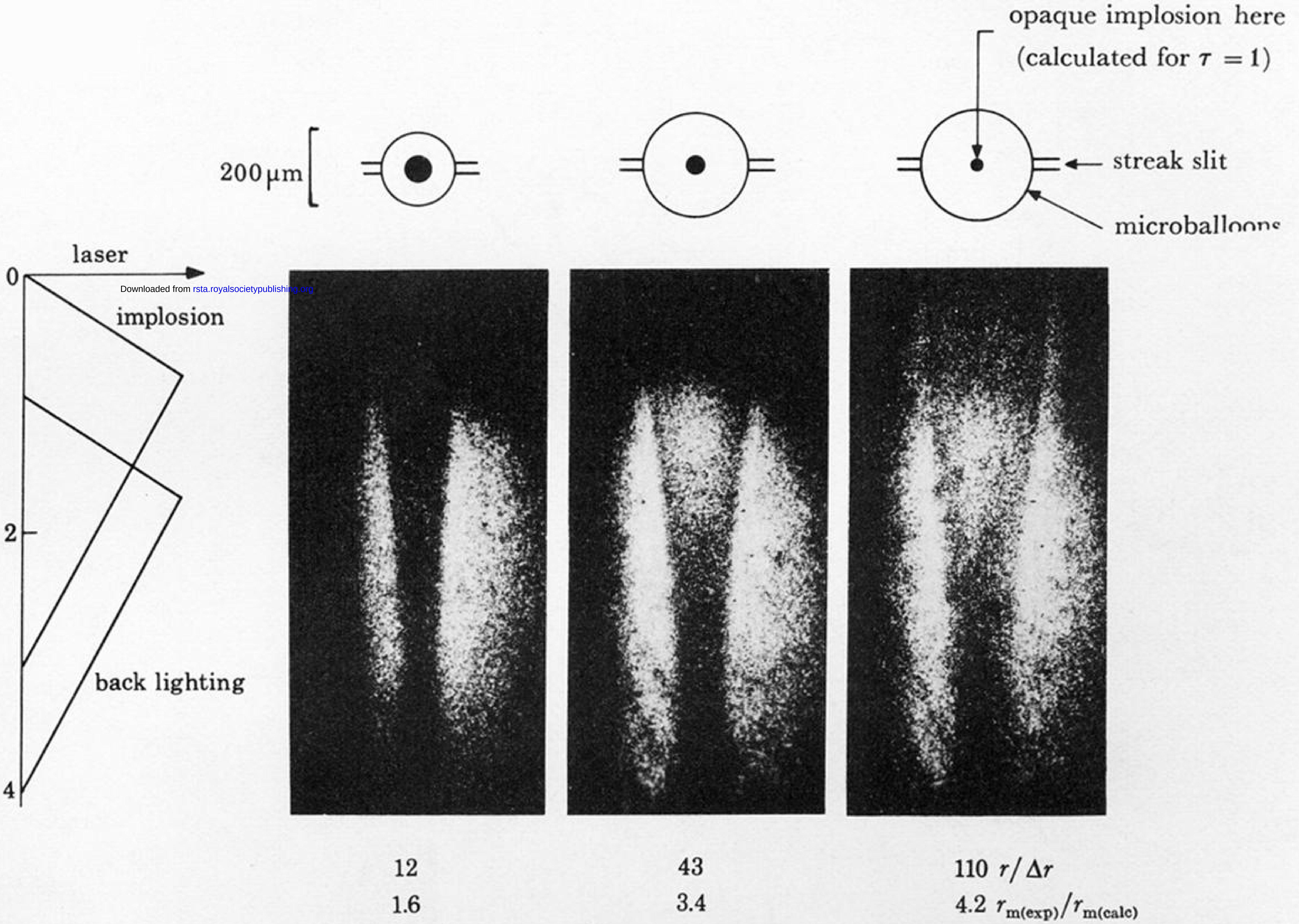

GURE 13. Three examples of ablative implosions diagnosed by streak time resolved X-ray shadowgraphy. The sketches above are scale drawings of the initial microballoon diameter, the streak slit and the computed size of the opaque compression core. The graph at the left side shows the relative timing of the irradiation of the microballoon and the back-lighting target. The streak pictures show the implosion trajectory and minimum size of the opaque core for shells of aspect ratio $r/\Delta r = 12$, 43 and 110. The ratio $r_{\mathrm{m\,(exp)}}/r_{\mathrm{m\,(calc)}}$ is that of observed to computed minimum opaque core size. (After Key *et al.* 1980.)